AGU ADVANCING EARTH AND SPACE SCIENCES

JGR Atmospheres

RESEARCH ARTICLE
10.1029/2025JD045737

The Relationship of Isolated Deep Convection Initiation to Orography and Sea Breezes Over Hainan Island and Leizhou Peninsula

Guilin Lu[1], Ke Cao[2], Shizuo Fu[3,4], Lanqiang Bai[5], Huiwen Xue[2], Zhiyong Meng[2], and Qinghong Zhang[2]

[1]Science and Technology Research Institute, China Three Gorges Corporation, Beijing, China, [2]Department of Atmospheric and Oceanic Sciences, School of Physics, Peking University, Beijing, China, [3]Key Laboratory for Humid Subtropical Eco-Geographical Processes of the Ministry of Education, Fujian Normal University, Fuzhou, China, [4]School of Geographical Sciences, Fujian Normal University, Fuzhou, China, [5]Foshan Tornado Research Center, Foshan Meteorological Service, Foshan, China

Key Points:

- Deep convection initiates over mountains and certain coastal plains over Hainan Island and Leizhou Peninsula
- The probability of deep convection initiation increases linearly with elevation, relief amplitude, and speed of sea breeze
- Deep convection initiation occurs over mountains in the late morning and extends to coastal plains in the afternoon

Correspondence to:

S. Fu,
fusz@fjnu.edu.cn

Citation:

Lu, G., Cao, K., Fu, S., Bai, L., Xue, H., Meng, Z., & Zhang, Q. (2026). The relationship of isolated deep convection initiation to orography and sea breezes over Hainan Island and Leizhou Peninsula. *Journal of Geophysical Research: Atmospheres*, *131*, e2025JD045737. https://doi.org/10.1029/2025JD045737

Received 27 OCT 2025
Accepted 6 APR 2026

Abstract

Hainan Island and Leizhou Peninsula in South China are characterized by abundant deep convection initiation (DCI), relatively complex orography, and strong sea breezes. This study uses the high-resolution (0.02° × 0.02°, 10-min interval) Himawari-8 satellite data to identify the isolated DCI events and employs statistical methods to relate the DCI occurrence to local orography and wind conditions. The statistics are based on 10,731 DCI events that occurred during the daytime of 412 locally forced DCI days in the warm seasons of 2016–2022. A 1-month WRF simulation, driven by the averaged reanalysis fields of these locally forced DCI days, is conducted to derive the local winds in the study area. The spatial distribution of DCI shows hotspots over mountains with high elevation and large relief amplitude, as well as over certain coastal plains experiencing strong sea breezes. DCI probability generally increases with elevation, relief amplitude, and speed of sea breezes, exhibiting significant linear correlations. The hotspots of DCI events tend to appear over mountains in the late morning and subsequently extend to coastal plains with strong sea breezes in the afternoon. The quantitative relationships established in this study provide useful insights for improving the forecasting of deep convection over tropical islands.

Plain Language Summary

Tropical islands are hotspots of thunderstorms. Using high-resolution satellite data, this study obtains the precise formation times and locations of thunderstorms that occurred over Hainan Island and Leizhou Peninsula in South China. The influence of orography and local winds on the spatiotemporal distribution of these thunderstorms is explored. Results show that thunderstorms prefer to form on high and steep mountains or coastal plains with strong sea breezes. Their occurrence frequency increases with the height and slope of mountains, as well as the speed of sea breezes over coastal plains. Thunderstorm hotspots over mountains generally occur earlier than those over coastal plains. These findings may help improve the forecasting of extreme weather, such as heavy rainfall and strong winds, over tropical islands.

1. Introduction

The initial formation of deep convective storms is often termed as deep convection initiation (DCI; Ziegler, 2014). DCI frequently occurs near synoptic-scale or mesoscale boundaries, where dynamic forcing and thermal circulations can lift air parcels to the level of free convection (Fu et al., 2021; Markowski & Richardson, 2010). When synoptic-scale forcing is weak, mesoscale boundaries produced by surface heterogeneities, such as orography, land-sea contrast, and soil moisture contrast, can induce local thermal circulations, thereby controlling the DCI process (e.g., Barthlott et al., 2016; Bennett et al., 2006; Guillod et al., 2015; Perlin & Alpert, 2001; Schneider et al., 2018). The ability to accurately predict the location and timing of DCI is crucial for the forecasting of subsequent extreme weather, such as heavy rainfall and strong winds. However, DCI processes associated with surface heterogeneities are often poorly predicted by current weather and climate models, due to an insufficient understanding and representation of initiation mechanisms in parameterizations, a lack of high-resolution observations for initial and boundary conditions, and a great computational expense associated with high-resolution simulations (Brunet et al., 2023; Schneider et al., 2018; Zadra et al., 2018).

For tropical islands, the strong thermal contrasts between the island and the surrounding sea give rise to land/sea breeze circulations, which dominate the diurnal cycle of convection initiation and precipitation (Carbone et al., 2000; Fovell, 2005; Qian, 2008). Island orography also impacts the convection initiation, as mountains dynamically alter the flow by lifting, deviation, or blocking, and thermally induce orographic circulations (e.g., Barthlott & Kirshbaum, 2013; Qian et al., 2012; Schneider et al., 2018). The impacts of sea breeze and orography on convection initiation have been intensively studied over tropical islands around the world, such as the Caribbean island of Dominica (e.g., Kirshbaum & Smith, 2009; Smith et al., 2009, 2012; Wang & Kirshbaum, 2015), the Hawaiian Islands (e.g., Esteban & Chen, 2008; Yang & Chen, 2008), and the Taiwan Island (e.g., Kuo & Chen, 1990; Yeh & Chen, 1998). The interaction of large-scale circulation with local sea-breeze circulation further complicates the thermodynamics over the island, and thus influences the subsequent initiation and evolution of deep convection (e.g., Nugent et al., 2014; Smith et al., 2012).

For the tropical islands in the South China Sea, deep convective storms frequently occur during the warm seasons, resulting in a substantial amount of precipitation (e.g., Bai et al., 2020a, 2020b; Li et al., 2021). Hainan Island and Leizhou Peninsula, surrounded by the South China Sea and characterized by relatively complex terrain, have increasingly drawn scientists' attention in recent years for studying the key factors regulating the initiation and evolution of deep convection (e.g., Liang & Li, 2024; Liang & Wang, 2017; Zhu et al., 2017, 2020). Previous real-case or semi-idealized simulations on Hainan Island have focused on the lifting caused by sea-breeze fronts, orography, or the combination of sea-breeze and valley-breeze circulations (Liang et al., 2017; Liang & Wang, 2017; Lu et al., 2025; Wang et al., 2018; Zhu et al., 2017, 2021). Over the Leizhou Peninsula, Fu et al. (2021) performed a semi-idealized simulation, and found that when a sea-breeze front collides with another sea-breeze front, or a preceding convective gust front, convection can be initiated. These studies theoretically explained how sea breezes and orography influence the diurnal cycle of DCI and precipitation over Hainan Island and Leizhou Peninsula.

Using observational data (such as rain gauge, radar, satellite, and reanalysis data), the spatiotemporal distribution of convection initiation and the corresponding environmental characteristics have been revealed from a long-term statistical perspective for the tropical islands in South China (e.g., Bai et al., 2020a, 2020b; Liang & Li, 2024; Liang & Wang, 2017; Zhu et al., 2020, 2021). For example, using a radar reflectivity criterion of 40 dBZ, previous studies have identified DCI events and shown hotspots over mountains and coastal areas of Hainan Island (Bai et al., 2020a, 2020b; Liang & Li, 2024; Zhu et al., 2021). Their findings also highlighted the impact of large-scale environmental winds and local circulations associated with land-sea contrast and orography on convection initiation and precipitation.

Satellite observations are another important data source that can be used to identify DCI, since it can reveal early stage cloud behaviors before the precipitation signal is captured by radars, and thus may provide additional lead time for DCI nowcasting (Huang et al., 2017). Moreover, satellite observations are insensitive to underlying orography, thereby avoiding the inaccuracies in ground-based radar observations caused by beam blockage over complex terrain. For example, Li et al. (2021) have identified deep convective systems over China using satellite data with a spatial resolution of 5 km and found that Hainan Island is one hotspot. The spatial and temporal resolution of satellite data is critical for accurate DCI identification. Previous studies have noted that the 5-km spatial and 30-min temporal resolution may be insufficient to resolve some DCI processes (Huang et al., 2017). Notably, Zhuge and Zou (2018) used the 1-km visible and 2-km infrared channels of Himawari-8 satellite at 10-min intervals to develop DCI nowcasting algorithms. However, their evaluation was based on only about two hundred DCI cases within a 3-month period, and they did not examine the long-term spatiotemporal characteristics of DCI using high-resolution satellite observations.

Previous simulation and statistical studies qualitatively examined the influence of surface heterogeneity, such as orography and sea breezes, on DCI events that occurred over Hainan Island and Leizhou Peninsula, and have provided valuable insights. However, their identification of DCI is constrained by the spatial and temporal resolution of data, which limits the ability to detect DCI at very early stages and with high precision. Moreover, the spatiotemporal distribution of DCI, as well as its quantitative relationships between DCI and relevant environmental factors (e.g., orography and sea breeze) have not been statistically established based on long-term high-resolution observations. In addition, the spatiotemporal characteristics of DCI over the Leizhou Peninsula remain relatively underexplored. In this study, we identify DCI events that occurred over Hainan Island and Leizhou Peninsula using the high-resolution Himawari-8 satellite data and explore the quantitative relationships of DCI

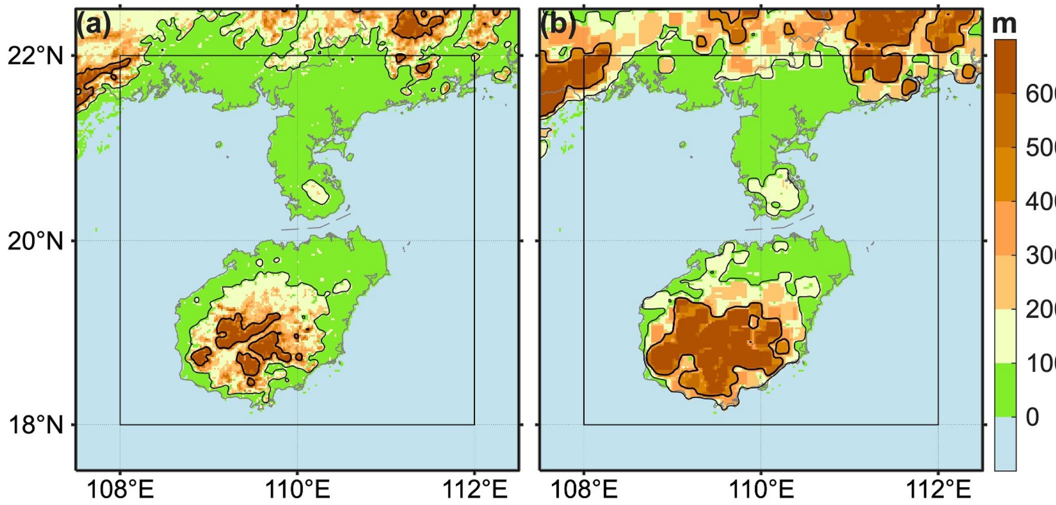

Figure 1. Maps of the study area. Panel (a) elevation (unit: m, mean sea level), and (b) relief amplitude (unit: m, mean sea level). The thin and thick black lines represent contours at 100 and 500 m, respectively.

with local orography and sea breeze strength. Section 2 introduces the data and methods used to identify DCI events, describe orography, and obtain local winds. Results are given in Section 3, including the spatiotemporal distribution of DCI events, and their relation to orography and sea breezes. The conclusions and discussions are in Section 4.

2. Data and Methods

2.1. Orography of the Study Area

The study area (inner domain in Figure 1a, 108°E–112°E, 18°N–22°N) mainly covers Hainan Island and Leizhou Peninsula. A larger area (outer domain in Figure 1a, 107.5°E–112.5°E, 17.5°N–22.5°N) is used for DCI identification in Section 2.2, since the clouds may cross the boundary of the study area during their evolution. This study uses elevation and relief amplitude to describe the orography, as was done by Lu et al. (2023). The Earth TOPOgraphy (ETOPO) 2022 elevation data (NCEI, 2022) with a resolution of 15 arc-sec (~0.46 km) is adopted and converted to 0.02° × 0.02° (~2 km × 2 km) to match the DCI locations obtained in Section 2.2. As shown in Figure 1a, Hainan Island is characterized by high inland mountains (~1.8 km) surrounded by plains. Across the narrow strait is the Leizhou Peninsula, featuring a small hill (~0.2 km) in the southern part.

Relief amplitude is used to quantify local variations of elevation and is defined as the difference between the maximum and minimum elevation within a moving window (Lu et al., 2023). The optimal window scale is determined by the elevation data resolution and the mean turning-point analysis (J. Zhang et al., 2018, 2019). In this study, the elevation resolution was 0.02° (~2 km), corresponding to an optimal window size of 7 × 7 grid points (~14 km × 14 km). This window effectively captures peak-to-valley terrain variations in the study area. As shown in Figure 1b, the spatial pattern of relief amplitude is similar to the elevation distribution in Figure 1a, but is overall smoother.

We simply categorize the study area into mountains, plains, and sea areas, based on elevation thresholds of 100 and 0 m. Specifically, sea areas are defined as regions with elevation below 0 m, following the conventional land–sea separation. Mountains are defined as areas with elevation greater than 100 m, which are also characterized by relatively large relief amplitude. Plains are defined as areas with elevation between 0 and 100 m, which are primarily located near the coasts and exhibit relatively small relief amplitude. The threshold of 100 m for mountain-plain classification leads to comparable areal coverage and DCI counts between mountains and plains, thereby ensuring the statistical reliability of the subsequent analyses. The choice of 100 m also allows small but dynamically important hills to be classified as mountains. These hills may significantly influence convective development (Antonelli & Rotunno, 2025), such as the hill in the southern Leizhou Peninsula (maximum height of about 200 m). Our previous study in North China has suggested that the dependence of DCI on elevation and relief amplitude varies among different types of orography (Lu et al., 2023). This study also relates DCI to

10.1029/2025JD045737

elevation and relief amplitude to quantify the effects of different orographies on DCI. We performed sensitivity tests by changing the threshold of mountain-plain classification to 50 m or 200 m. The number of grid points and the DCI counts over each terrain type are changed, but the DCI density and the associated quantitative relationships remain unchanged. Therefore, we only show the results using the 100 m threshold.

2.2. Identification of DCI Events

DCI is identified using the visible reflectance (0.47-μm) and infrared brightness temperature (BT, 10.4-μm) from the Himawari-8 satellite with a horizontal resolution of $0.02° \times 0.02°$ ($\sim$2 km × 2 km) and a temporal resolution of 10-min (Bessho et al., 2016). The study period covers the warm seasons (May to September) of 2016–2022. As in Lu et al., 2023, the locally forced days are selected to focus on local forcings associated with surface heterogeneities. The locally forced DCI days were manually selected by screening the hourly visible images of Himawari-8 satellite. A day is considered as a locally forced DCI day if at least one isolated, very bright cloud forms within the study area, while no larger-scale cloud systems, such as typhoon-related or frontal clouds characterized by elongated or rotating structures, affect the region throughout the day. A total of 412 days was selected. These days are characterized by clear skies or shallow cumuli in the morning, followed by isolated DCI occurrence in the rest of the day. Since most DCI events in South China occur during the daytime (Bai et al., 2020a), this study only identifies daytime (08:00–18:00 LST) DCI events.

The DCI identification procedure in this study is built upon an algorithm that we previously developed for the North China area (Lu et al., 2023). However, following Zhuge and Zou (2018), the procedure uses the visible channel to exclude cirrus, applies a higher BT threshold, and adopts a higher spatial resolution to more accurately identify deep convection initiation for the tropical islands in Southern China. Specifically, isolated deep convective clouds are identified in each 10-min satellite scene using a multi-step procedure. Cold cloud regions are first detected as contiguous areas with BT lower than 273 K and reflectance greater than 0.35. To ensure that the cold cloud systems are isolated, only those spanning an area of less than 250 pixels ($\sim$1,000 km^2) are retained. Among these isolated cold clouds, those containing a core colder than 253 K and larger than 2 pixels ($\sim$8 km^2) are defined as isolated deep convective clouds. Using Level-2 cloud product data of Himawari-8 satellite, cloud-top heights (CTH) are computed for several representative DCI days (e.g., 23–26 September 2018). The mean CTH of the entire isolated deep convective clouds ($\leq$273 K) is approximately 8–9 km, while the mean CTH of the cold-core regions ($\leq$253 K) reaches 9–10 km, consistent with expectations for deep convective cloud development.

These isolated deep convective clouds are then tracked across consecutive scenes using the temporal overlapping method (Zhuge & Zou, 2018; Zinner et al., 2008), which regards a cloud in the current scene as the same cloud from the previous scene if there is an overlap between them. To ensure that these isolated deep convective clouds are developing upward, we track them in three consecutive scenes, and require their cloud top to consistently maintain a cooling rate greater than 2.7 K per 10 min throughout these scenes. The cloud top temperature of each isolated deep convective cloud is represented by the average BT of the coldest 25% of the cloud pixels (Walker et al., 2012). Given the 10-min temporal resolution, this cooling rate criterion requires a minimum lifetime of longer than 20 min. Gupta et al. (2024) documented that isolated deep convective cells typically persist for about 70 min, suggesting that this threshold is expected to capture most DCI events.

Finally, each developing deep convective cloud, defined as a DCI event, is tracked back to the scene where it first meets the development criteria, which is marked as its initiation time. The geometric center of the cloud is taken as the DCI location. Following the aforementioned criteria, a total of 10,731 isolated DCI events were identified on the 412 locally forced days. In the following sections, statistical analyses are employed to relate the spatio-temporal distribution of these DCI events to local orography and local winds.

2.3. Local Winds

The Weather Research and Forecasting (WRF v4.5, Skamarock et al., 2008) model, configured with specially designed initial and lateral boundary conditions, is used to simulate the local circulation. The global final analysis data (FNL, $1° \times 1°$, NCEP, 2000) at 08:00, 14:00, 20:00, and 02:00 LST are averaged over the 412 locally forced DCI days. This averaging removes day-to-day synoptic variability and yields a representative mean large-scale background environment. Using these averaged FNL fields, the simulation is initialized at 08:00 LST, with the lateral boundary conditions being updated at the aforementioned four times. The same lateral boundary conditions were repeated every day over a period of 30 days. Because the lateral boundary forcing is identical from day-to-

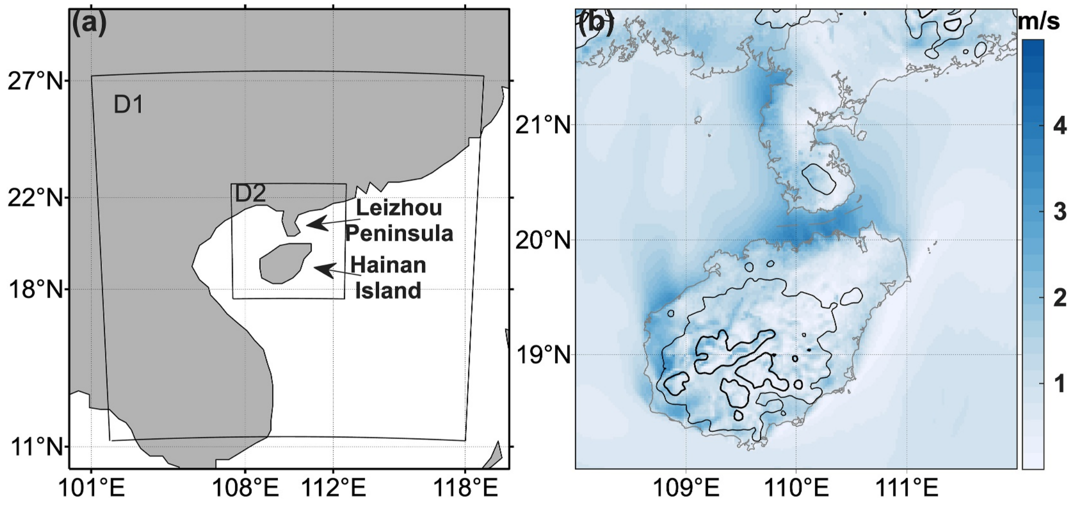

Figure 2. (a) Domain configuration of the WRF simulation, with the inner domain D2 focusing on Hainan Island and Leizhou Peninsula. D2 is approximately the same as the outer domain of Figure 1a. Panel (b) Wind speed of the daytime-averaged (08:00–18:00 LST) local winds at 10 m height. The thin and thick black lines represent contours of elevation at 100 and 500 m, respectively.

day, the simulated diurnal evolution becomes highly repetitive after the initial spin-up, exhibiting the mean diurnal response to thermally driven local circulations (e.g., land–sea breezes or terrain-induced circulations), rather than to individual weather events (e.g., typhoon and frontal systems). This experimental design follows prior semi-idealized or climatological WRF frameworks (e.g., Bao & Zhang, 2013; Chen et al., 2017; Trier et al., 2010; Y. Zhang et al., 2013; Zhu et al., 2017, 2021). For example, Zhu et al. (2017, 2021) used a 10-year-averaged reanalysis data as initial and lateral boundary conditions. They found that the repeatedly developing thermally driven activities, such as land-sea breezes, are well captured by WRF simulations, while transient atmospheric perturbations can be filtered out.

As shown in Figure 2a, two nested domains are used, with the inner domain focusing on the Hainan Island and Leizhou Peninsula. The outer domain (D1) and inner domain (D2) have 180 × 180, 271 × 281 grid points with horizontal grid spacings of 10 and 2 km, respectively. A total of 50 vertical levels were set with the model top at 50 hPa. The Yonsei University (YSU) boundary layer scheme (Hong et al., 2006), the Dudhia shortwave radiation scheme (Dudhia, 1989), the Rapid Radiative Transfer Model longwave radiation scheme (Iacono et al., 2008), and the single-moment 6-class microphysics (Hong & Lim, 2006) are used for both domains, while no cumulus parameterization is used. The simulation was integrated for 30 days, and the first 2 days were considered as spin-up time. The wind field data is recorded every 10 min, and the hourly mean wind is used to analyze the local winds.

The hourly mean wind fields contain multiscale motions, including large-scale synoptic winds and the local-scale winds such as sea breezes. Therefore, the daily mean wind vectors, regarded as synoptic winds, are subtracted from the hourly mean wind vectors to approximately obtain the local wind vectors, which exhibit a much more prominent diurnal variation (Liang & Wang, 2017; Zhu et al., 2017). The local winds are further averaged over the 28 simulation days to mitigate day-to-day variations. Figure 2b shows the spatial distribution of the simulated daytime-averaged 10-m local wind speed, which is calculated using the simulated local wind vectors. Strong local winds are mainly along the northern coastline of Hainan Island and the western side of the Leizhou Peninsula, particularly near the narrow strait between them, as well as over certain inland mountainous regions. It should be emphasized that the wind fields shown in Figure 2b are averaged on all locally forced DCI days across Hainan Island and the surrounding areas, and are not of any individual weather event.

The simulated pattern of local winds in Figure 2b is generally similar to that reported in previous studies over Hainan Island or South China (e.g., Chen et al., 2016; Duan et al., 2023; Huang et al., 2016; Tu et al., 1993; Z. Z. Zhang et al., 2014). Particularly, Chen et al. (2016) showed that sea-breeze circulations in South China are primarily established over low-lying coastal plains and typically confined below 200 m, whereas inland

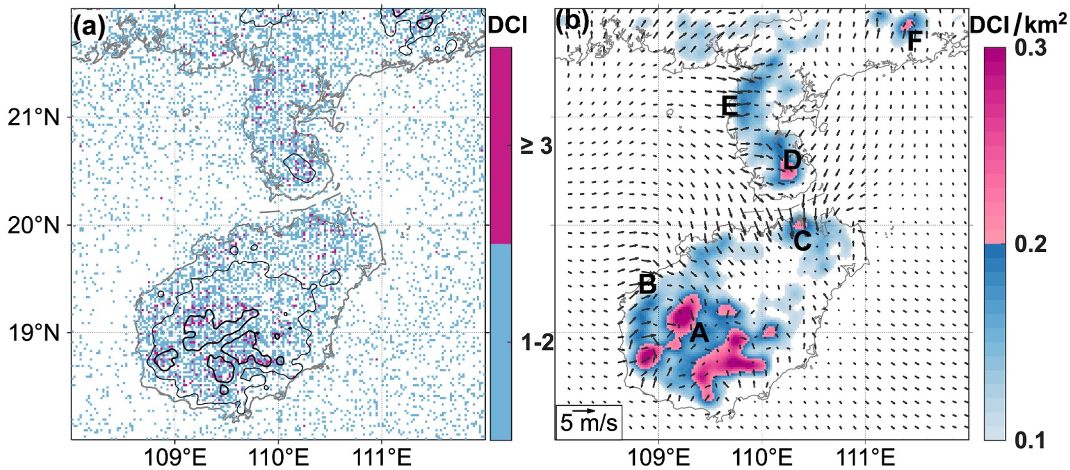

Figure 3. Spatial distribution of the 10,731 isolated DCI events. Panel (a) counts of DCI events at each 0.02° × 0.02° grid point. Blue dots indicate that there are only 1 or 2 DCI events in these grid points, while pink dots indicate 3 or more DCI events. The thin and thick black lines represent contours of elevation at 100 and 500 m, respectively. Panel (b) density of DCI events (DCI events per square kilometer) from the two-dimensional kernel estimation (filled color contours) and wind vectors of the daytime-averaged (08:00–18:00 LST) local winds. Note that the wind field here is the same as that shown in Figure 2b, but it is represented by vectors here.

mountainous regions near the coastlines are mainly influenced by mountain–plain solenoids. Here, we adopt a simplified interpretation in which daytime local winds over coastal plains and adjacent oceanic areas are assumed to be primarily associated with sea breezes, whereas local winds over inland mountainous regions are mainly governed by slope winds. Accordingly, sea breezes hereafter refer to the local winds over plains and oceanic areas, whereas slope winds refer to the local winds over mountainous regions. In the following sections, we focus on the relationship between this average wind field and the overall DCI spatial distribution, rather than on the one-to-one correspondence between real-time winds and individual DCI events.

3. Results

3.1. The Spatial Distribution of DCI Events

Figure 3 shows the spatial distribution of the 10,731 DCI events identified in Section 2.2 . Grid points with three or more DCI events (pink dots in Figure 3a) are generally located over mountains and certain coastal plains. This characteristic of the DCI hotspots is illustrated more clearly by the DCI density in Figure 3b, which is calculated using the two-dimensional kernel density estimation (KDE) and quantifies the number of DCI events per unit area. High DCI density is seen over mountainous regions with relatively higher elevations, such as the mountains of Hainan Island (area A), the hill in the southern Leizhou Peninsula (area D), and the hills of the South China mainland (area F).

The coastal plains in the southwest (area B) and northeast (area C) of Hainan Island, as well as the western coastlines of Leizhou Peninsula (area E), also exhibit high DCI density. These coastal DCI hotspots highly overlap with areas where strong local winds develop, as shown by the black arrows in Figure 3b. The spatial distribution of DCI events in Figure 3b closely aligns with the patterns derived from radar observations (e.g., Bai et al., 2020a) and low-resolution satellite observations (e.g., Li et al., 2021). Compared with radar-based studies, Figure 3b shows more pronounced DCI hotspots over mountainous regions, likely because satellite-based identification can avoid the underestimation of DCI events over complex terrain associated with terrain-induced radar beam blockage. Compared with low-resolution satellite-based studies, Figure 3b exhibits finer details of DCI occurrence. In particular, evident contrasts in DCI density between mountain peaks and foothills on Hainan Island, and similarly sharp variations are observed across the narrow Leizhou Peninsula. The enhanced detection of mountainous DCI in our results therefore highlights key advantages of high-resolution satellite-based DCI identification, particularly in regions with complex terrain. The fine-scale DCI spatiotemporal distribution at a high resolution of 0.02° × 0.02° is used to quantify the relationship between DCI occurrence and orography, as well as local winds.

Table 1
DCI Counts, Area, and DCI Probability (DCI Events per Square Kilometer) for the Entire Domain and Three Orographic Types

	DCI counts	Area (km^2)	DCI probability (DCI/km^2)
Domain	10,731	161,604	0.07
Mountains	3,302	17,836	0.19
Plains	4,338	39,612	0.11
Sea	3,091	104,156	0.03

3.2. Relation of DCI to Orography

The spatial distribution of DCI shown in Figure 3 indicates pronounced differences in the occurrence probability across different orographic types. To quantitatively characterize these differences, Table 1 presents the DCI counts and their corresponding occurrence probabilities for the entire domain as well as for each orographic type. The DCI probability is defined as the number of DCI events normalized by the area of the corresponding orographic type. For the entire domain, the DCI probability is approximately 0.07 DCI events per square kilometer. The DCI probability is much higher over mountains compared to that over coastal plains and sea areas. This indicates that mountainous areas are more favorable for the occurrence of DCI events than coastal plains.

To quantitatively evaluate whether the terrain characteristics at locations where DCI events occur differ statistically from the background terrain of the study area, Table 2 presents the mean values of elevation and relief amplitude, along with the results of the *t*-tests. Specifically, for the entire domain, mountains, and plains, the mean elevation (and relief amplitude) at DCI locations are calculated and compared with the corresponding mean values of the entire domain or of the same orographic type. Two-sample *t*-tests are further applied to assess the statistical significance of these differences (O'Mahony, 1986; Student, 1908). As an illustrative example, the first row of Table 2 shows that the mean elevation of all DCI events over the entire domain is 133 m, substantially higher than the domain-mean elevation of 43 m. The p value (<0.01) indicates that this difference is statistically significant at the 0.05 significance level. Similar statistically significant differences were found for the relief amplitude.

Overall, for DCI events occurring in the entire domain and in mountains, both mean elevation and mean relief amplitude are significantly higher than their respective background values, indicating a clear preference for elevated and topographically complex terrain. In contrast, over plains, where relief amplitude exhibits limited spatial variability, the mean relief amplitude of DCI events does not differ significantly from that of all plain areas, despite slightly higher elevation.

These differences indicate that DCI events are not randomly distributed with respect to terrain, but are preferentially associated with regions of higher elevation and greater relief amplitude. To quantitatively evaluate the relations of DCI to elevation and relief amplitude, we conducted the linear regression analyses with the function $Y = \beta_0 + \beta_1 X + \varepsilon$, where β_0 (intercept) and β_1 (slope) are the regression coefficients, and ε represents the random error. Elevation and relief amplitude are segmented into bins with a width of 100 m, ensuring sufficient DCI events in each bin for statistically robust regression. The DCI probability in each bin is adopted as the response variable (Y), and the corresponding elevation or relief amplitude is used as the explanatory variable (X), respectively. A strong and statistically significant linear relationship between the response and explanatory variables is considered to exist when the regression slope (β_1) is large, the goodness of fit (R^2) approaches 1, and the p value is less than 0.05 (Chatterjee & Hadi, 2006; Lu et al., 2023). Sensitivity tests suggest that the conclusions are qualitatively the same when the bin width is changed from 100 to 200 m (not shown).

As shown in Figure 4a, DCI probability increases monotonically with elevation. The linear relationship between DCI probability and elevation is strong and statistically significant at a significance level of 0.05. A significant

Table 2
Comparisons of Mean Elevation and Mean Relief Amplitude (RA) for DCI Events Occurring in the Entire Domain, Mountains, and Plains, Versus the Mean Elevation and Mean Relief Amplitude for the Entire Domain or the Corresponding Orographic Type

	Mean elevation (m)	p value	Mean RA (m)	p value
Total DCI events versus entire Domain	133 versus 43	$\mathbf{p < 0.01}$	236 versus 87	$\mathbf{p < 0.01}$
DCI events over mountain areas versus mountain areas	382 versus 315	$\mathbf{p < 0.01}$	613 versus 529	$\mathbf{p < 0.01}$
DCI events over plain areas versus plain areas	38 versus 35	$\mathbf{p < 0.01}$	118 versus 118	$p = 0.49$

Note. The p values are obtained from the two-sample t-test, with those in bold denoting statistical significance at a 0.05 significance level.

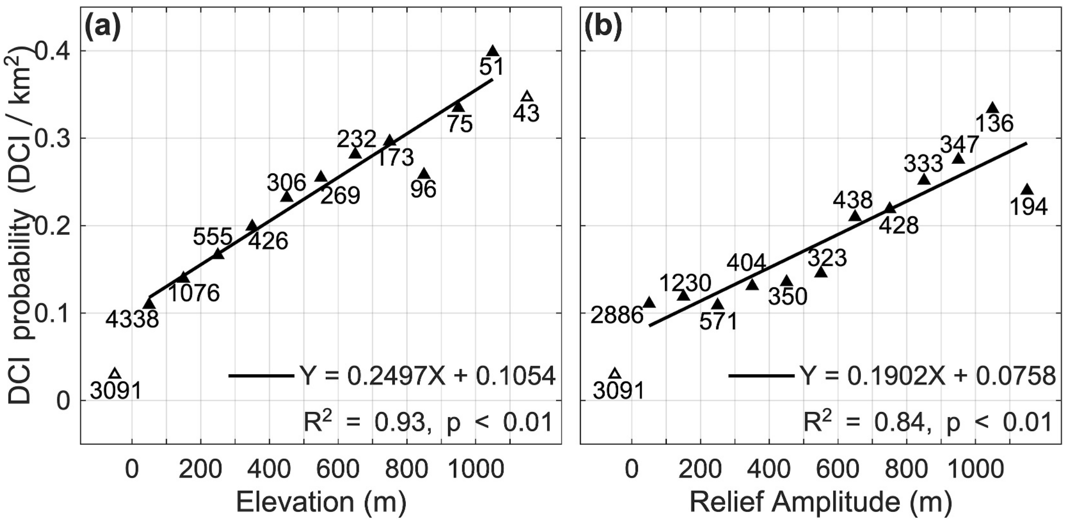

Figure 4. Relationship between DCI probability (DCI events per square kilometer) and (a) elevation, and (b) relief amplitude. The triangles indicate the mean DCI probability for each bin: filled triangles represent bins with elevation above 0 m and more than 50 DCI events, while open triangles indicate bins with elevation below 0 m or fewer than 50 DCI events. The number of DCI events in each bin is labeled adjacent to each triangle. The black line shows the result of linear regression conducted using these filled triangles. The regression equation, goodness of fit (R^2), and p-value are indicated in each panel.

correlation between DCI probability and relief amplitude also exists (Figure 4b). Compared with elevation, the linear relationship between DCI and relief amplitude is weaker, with relatively smaller goodness of fit R^2 and regression slope β_1. In the study area (Figure 1), the mountainous regions with high elevation correspond to large relief amplitude, while the coastal plains have relatively low elevation and small relief amplitude (Figures 1a and 1b). This suggests that only one of elevation or relief amplitude, may be needed in practical applications for regions like Hainan Island. However, in other regions, the relationships among these variables may differ substantially. For example, over North China, DCI exhibits more complex relationships with elevation and relief amplitude (Lu et al., 2023). This highlights the need to consider the combined effects of elevation and relief amplitude when assessing the probability of DCI occurrence.

3.3. Relation of DCI to Local Winds

To examine the impacts of local winds on DCI probability, we classified local wind conditions as either weak-wind (<1.44 m/s) or strong-wind (≥1.44 m/s). The threshold is chosen based on the 10-m local wind speed averaged over the daytime and the entire domain. Using this threshold and the daytime-averaged local winds shown in Figure 2b, each grid point in the study area can be classified into areas of weak wind or areas of strong wind. As shown in Table 3, the DCI probability in strong-wind areas is approximately twice that in weak-wind areas, although the total number of DCI events is nearly identical in both categories. The daytime-averaged and domain-mean wind speeds for all DCI events is 1.56 m/s. Results from a two-sample *t*-test indicate that the mean local wind speed of all DCI events is significantly higher than the entire-domain average, further confirming that DCI events are more likely to occur in areas with stronger local winds.

Table 3
The Second to Fourth Columns Are Comparisons of DCI Events, Area, and DCI Probability Between Weak Winds and Strong Winds, Respectively

	DCI counts	Area (km^2)	DCI probability (DCI/km^2)	Mean local wind (m/s)	*p* value
Weak wind areas	5,583	104,760	0.05	1.56 versus 1.44	$\mathbf{p < 0.01}$
Strong wind areas	5,148	56,844	0.09		

Note. The last two columns show the comparison of mean wind speed of all DCI events versus the entire-domain average, and the bolded *p* value suggests a statistically significant comparison.

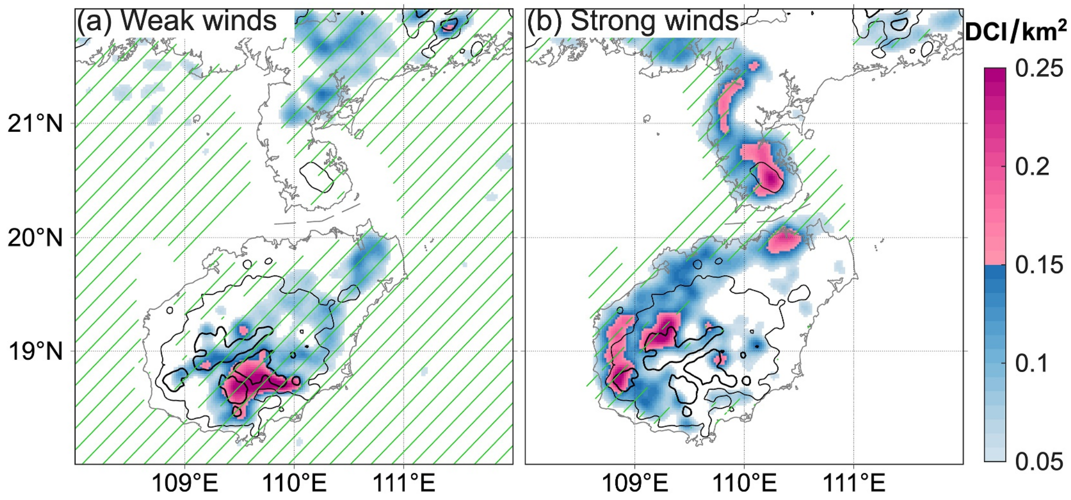

Figure 5. DCI density for (a) weak winds, and (b) strong winds. The thin and thick black lines represent contours of elevation at 100 and 500 m, respectively. The overlaying green hatching lines denote the regions of weak winds and strong winds, respectively.

As shown in Figure 5a, under weak local winds, DCI events are mainly concentrated over the mountains in Hainan Island. In these regions, upslope winds are produced when solar radiation heats the slopes. The convergences of upslope winds play dominant roles in initiating convection (Gong et al., 2025). When the local winds are stronger (Figure 5b), DCI hotspots are mainly located over the coastal plains of Hainan Island and the Leizhou Peninsula, indicating a stronger influence of sea-breeze–induced low-level convergence and lifting over flat coastal terrain.

Regression analyses show no significant linear relationship between DCI probability and local wind speed for DCI events occurring over the entire domain (Figure 6a) or over the mountains (orange line in Figure 6b) at the 0.05 significance level. However, for DCI events occurring over plains (green line in Figure 6b), DCI probability increases monotonically with the wind speed, and the linear relationship is statistically significant. This correlation indicates that local winds, particularly in the form of sea breezes, substantially influence DCI occurrence over low-lying coastal plains on tropical islands (e.g., area C and E in Figure 3b).

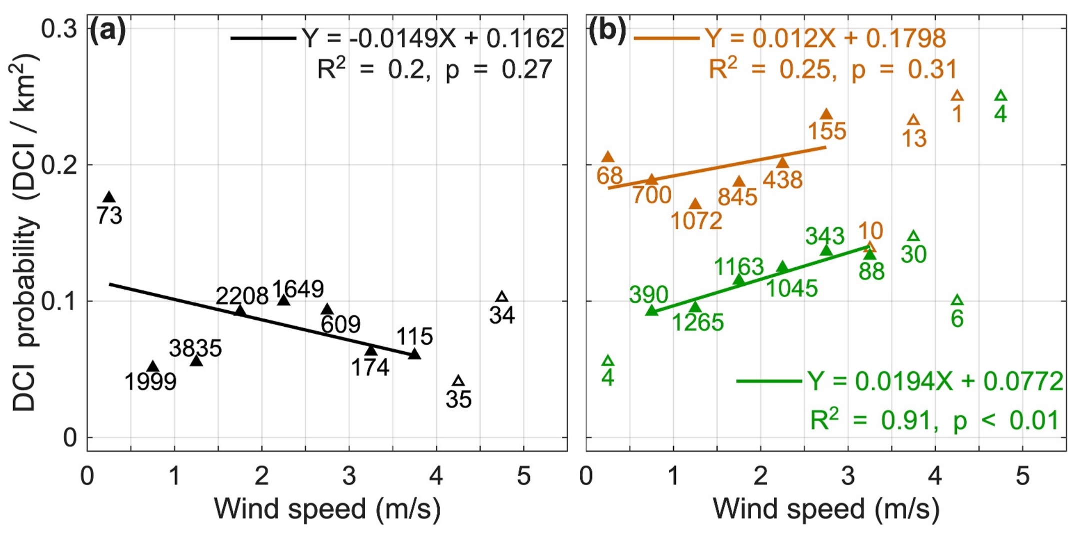

Figure 6. Relationships between DCI probability (DCI events per square kilometer) and local wind speed for DCI events occurring over (a) the entire domain, and (b) mountains (orange) and coastal plains (green). The lines show the results of linear regressions conducted using these filled triangles, which represent bins with more than 50 DCI events.

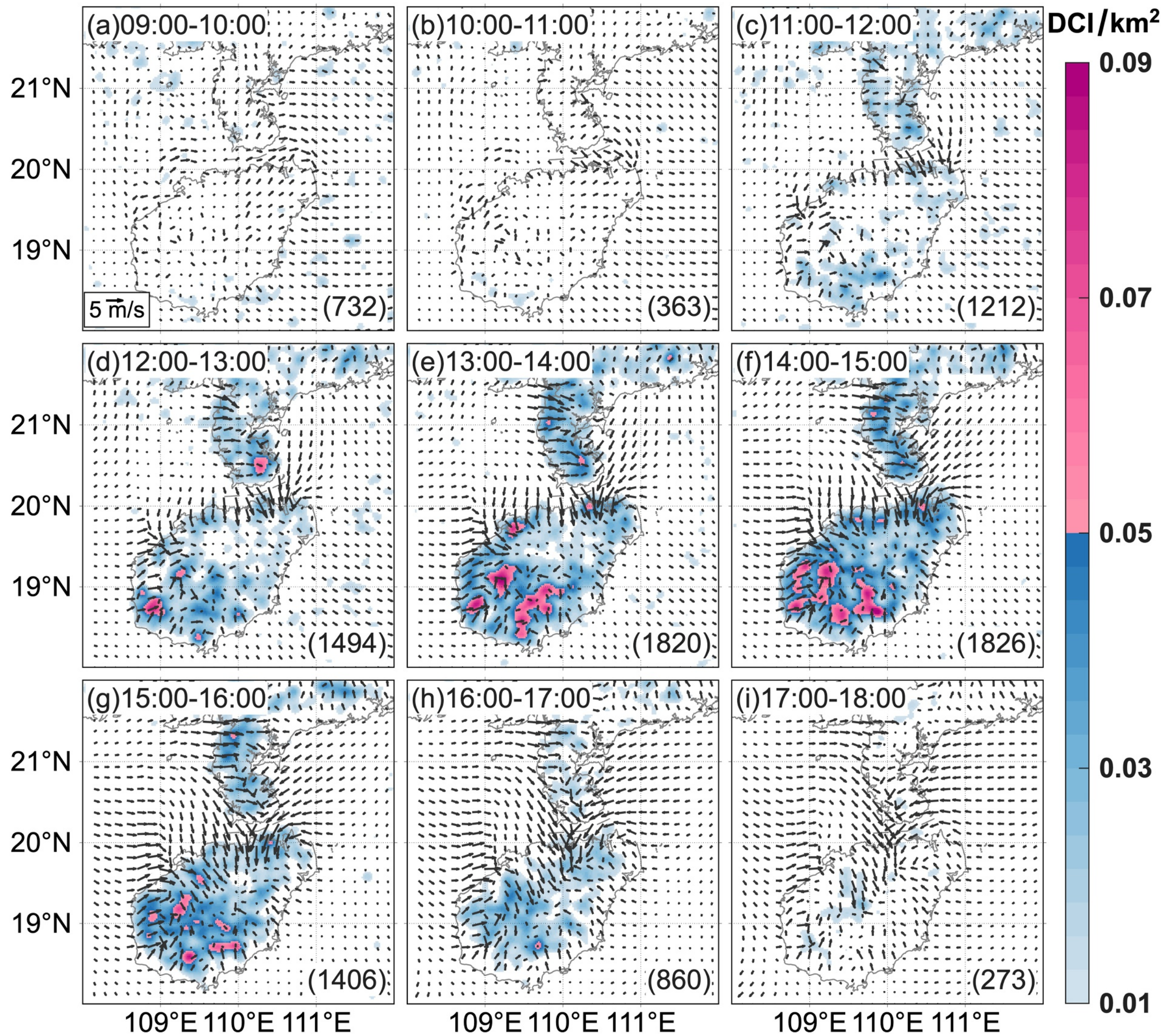

Figure 7. Hourly DCI density (filled color contours) and vectors of local winds during 09:00–18:00 LST. The number at the bottom right corner of each panel denotes the hourly DCI counts of the entire domain.

3.4. Temporal Distribution of DCI Events

The DCI time varies among the DCI hotspots. To illustrate such variation, we calculated the KDE-estimated DCI density at each hour and showed it in Figure 7. Most DCI events take place between 11:00 and 17:00 LST. During this period, the locations of DCI hotspots shift continuously as the sea breezes gradually intensify, moving toward the center of the island and peninsula.

In the morning (09:00–11:00 LST, Figures 7a and 7b), local winds are weak, and only a few DCI events occur, evenly distributed across the study area. Around noon (11:00–13:00 LST, Figures 7c and 7d), local winds start to gradually intensify due to solar heating, and low DCI frequency appears near the coastlines. Meanwhile, higher DCI frequency starts to form over the mountains in the southwest of Hainan Island, away from regions affected by strong sea breezes. The acceleration of DCI by mountains has also been reported by Lu et al. (2025) using semi-idealized WRF simulations. From afternoon to evening (13:00–18:00 LST, Figures 7e–7i), sea breezes further strengthen and propagate inland, with the sea-breeze convergence zone gradually shifting from northern to central Hainan Island. The convergence and associated lifting promote frequent DCI occurrences near the coastlines, which then exhibit a tendency to migrate inland in the late afternoon. During this period, DCI continues to frequently occur over the mountains.

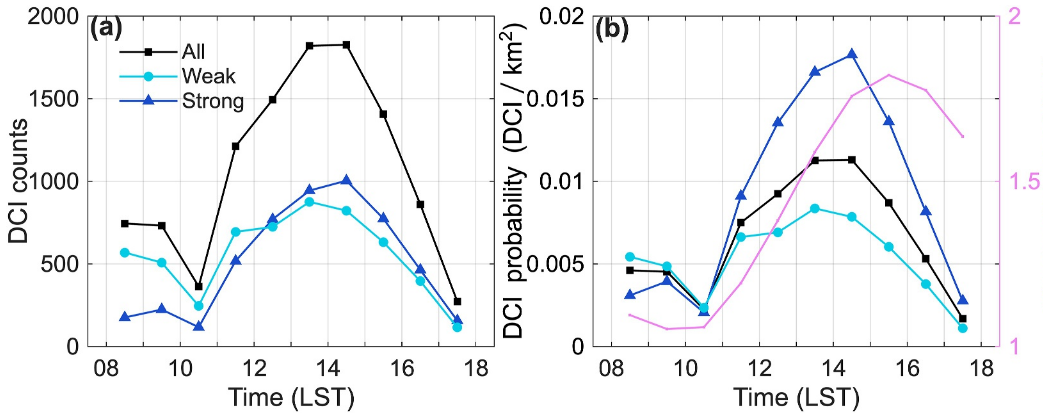

Figure 8. Temporal variation of (a) DCI counts, and (b) DCI probability (DCI events per unit area) for all the DCI events (black), DCI events under weak local winds (light blue), and DCI events under strong local winds (dark blue). The pink line in (b) is the domain-averaged hourly 10-m wind speed.

On the Leizhou Peninsula, the small hill in the south first initiates convection before 13:00 LST (Figure 7d). In the afternoon (Figures 7e–7g), sea-breeze fronts continuously collide over the central part of the peninsula, forming a persistent convergence zone. This leads to sustained DCI occurrence over the central peninsula, with a tendency to expand from south to north. The observed spatiotemporal evolution of DCI on the Leizhou Peninsula is broadly consistent with a previous idealized modeling study, which reported that orography of modest height (∼200 m) can force deep convection to develop before the collision of sea-breeze fronts at the peninsula center (Antonelli & Rotunno, 2025). Our results further highlight how small-scale topography modulates both the timing and preferred locations of DCI under realistic environmental conditions.

The temporal variation of DCI frequency shows that mountains and the associated relatively weak upslope winds are responsible for early DCI occurrences. In the afternoon, however, relatively strong sea breezes play crucial roles in DCI over the coastal plains. Figure 8 illustrates the temporal variation of DCI events under weak- and strong-wind conditions. The number of DCI events under weak winds is higher before noon, and becomes slightly lower than that under strong winds in the afternoon (Figure 8a). The local minimum in DCI counts between 10:00 and 11:00 LST is likely related to a routine data gap in Himawari-8 observations due to the daily housekeeping, which may have led to missed detection of DCI events occurring at or near that time.

Figure 8b further shows the DCI probabilities under weak winds, strong winds, and all conditions, which are the hourly DCI counts in Figure 8a divided by the areas under each wind condition. Consistent with the DCI counts in Figure 8a, the DCI probability under weak winds reaches a maximum between 13:00 and 14:00 LST, and remains at a relatively high value thereafter. In contrast, the DCI probability under strong winds peaks about 1 hr later, between 14:00 and 15:00 LST, and then gradually decreases. The distribution of all DCI events closely follows that of strong winds. Overall, after 11:00 LST, the DCI probability under strong winds is substantially higher than that under weak winds, indicating that more DCI events occur in areas with strong winds. The domain-averaged hourly local wind speed shown in Figure 8b (pink line) peaks approximately 1 hr later than the DCI probability of strong wind, suggesting that the sea-breeze circulation plays an important role in modulating DCI evolution in the afternoon.

4. Conclusions and Discussions

This study investigates the statistical characteristics of isolated DCI events and their relation to orography and local winds over Hainan Island and Leizhou Peninsula during the warm seasons of 2016–2022. The high-resolution (0.02° × 0.02°, 10 min) Himawari-8 satellite data were used to manually select the locally forced DCI days and automatically identify DCI events. The timing and locations of 10,731 DCI events that occurred during the daytime of 412 locally forced DCI days were collected and further related to the orography and local winds in the study area. The orography of the study area is described with elevation and relief amplitude. The general pattern of local winds is derived from a 1-month WRF simulation, which is initialized with the averaged reanalysis fields of the 412 locally forced DCI days.

DCI hotspots are distributed over mountains and certain coastal plains of Hainan Island and Leizhou Peninsula. The DCI probability over mountains is greater than that over plains. Comparisons conducted with *t*-tests suggest that DCI events tend to occur at areas with high elevation and large relief amplitude. Linear regression analyses further suggest that the DCI probability increases linearly with elevation and relief amplitude, and the linear relationships between them are strong and statistically significant.

On average, stronger local winds are associated with a higher DCI probability. For DCI events occurring over coastal plains, the DCI probability increases monotonically with wind speed, and the linear relationship between them is statistically significant. However, for DCI events occurring across the entire domain or over the mountains, there is no significant linear relationship between DCI probability and local winds. This suggests that researchers should consider the influence of sea breezes on DCI, especially in the low-lying coastal plains of tropical islands. Over these regions, daytime thermal contrasts between land and sea drive onshore sea-breeze flows, and the associated low-level convergence and lifting can become the dominant mechanism for convection initiation. Note that the upslope winds also facilitate the occurrence of DCI over mountainous regions. However, the speed of the slope winds is generally slower compared to the sea breezes, and the quantitative relationship between the slope winds and DCI density is much more complicated and requires further investigation.

The temporal distribution of DCI events indicates that the main period for DCI occurrence is during 11:00–17:00 LST. Deep convection tends to occur earlier over the mountains in the southwest of Hainan Island and the south of the Leizhou Peninsula, where local winds are weak. In the afternoon, DCI events are observed both in the mountains and in some areas of the coastal plains. On days when local forcing dominates, the intense solar radiation induces upslope winds over mountainous regions and sea breezes around coastal areas, both of which promote the initiation of deep convection.

These results reveal that the DCI occurrence is closely controlled by the small-scale orography and local wind circulation. Mountains trigger early daytime convection through thermally driven upslope winds, while sea breezes dominate afternoon DCI over coastal plains, highlighting the spatiotemporal organization of convective initiation at fine scales. This study underscores the importance of high-resolution observations and modeling in capturing these local effects, which are often unresolved in coarse data sets. Understanding these dynamic-thermodynamic couplings provides critical guidance for improving the prediction and monitoring of localized convective hazards in tropical coastal regions. On the other hand, DCI remains challenging for both weather forecasting and climate projection. For weather forecasting, our results suggest that more attention should be paid to the coastal regions and the mountainous regions to better understand and forecast DCI. In climate models, the quantitative relationships established in this paper can be used to improve cumulus parameterization schemes. For example, multiple regulatory factors reflecting the increased probability of DCI occurrence—such as elevation rise, increased relief amplitude, or strengthened local winds—could be incorporated into the trigger function of cumulus parameterization.

Conflict of Interest

The authors declare no conflicts of interest relevant to this study.

Availability Statement

The visible (band 1, 0.47 μm) and infrared (band 13, 10.4 μm) satellite data used in this study are from Himawari-8 satellite (The download URL is https://www.eorc.jaxa.jp/ptree) supplied by the P-Tree System, Japan Aerospace Exploration Agency (JAXA). The elevation data used in this study is the ETOPO2022 data (The download URL is https://www.ncei.noaa.gov/products/etopo-global-relief-model) published by the NCEI (2022). The $1° \times 1°$ global final analysis FNL data from the NCEP (2000) can be downloaded from https://rda.ucar.edu/datasets/d083002/. The WRF model is publicly available at https://www.mmm.ucar.edu/models/wrf. The DCI location and time data set presented in this paper (Lu, 2026) is available at https://zenodo.org/records/18368323. Other data from the identification procedures and WRF simulations are stored locally and can be provided to interested readers upon request to the lead author.

Acknowledgments

This work is supported by National Key Research and Development Program of China (Grant 2024YFF0809402) and National Natural Science Foundation of China (Grant 42275006, 41930968 and 42175091).

References

Antonelli, M., & Rotunno, R. (2025). Effect of orography on deep convection initiation produced by two sea-breeze fronts. *Journal of the Atmospheric Sciences*, *82*(10), 2219–2236. https://doi.org/10.1175/jas-d-24-0254.1

Bai, L. Q., Chen, G. X., & Huang, L. (2020a). Convection initiation in monsoon coastal areas (South China). *Geophysical Research Letters*, *47*(11), e2020GL087035. https://doi.org/10.1029/2020gl087035

Bai, L. Q., Chen, G. X., & Huang, L. (2020b). Image processing of radar mosaics for the climatology of convection initiation in South China. *Journal of Applied Meteorology and Climatology*, *59*(1), 65–81. https://doi.org/10.1175/jamc-d-19-0081.1

Bao, X., & Zhang, F. (2013). Impacts of the mountain–plains solenoid and cold pool dynamics on the diurnal variation of warm-season precipitation over northern China. *Atmospheric Chemistry and Physics*, *13*(14), 6965–6982. https://doi.org/10.5194/acp-13-6965-2013

Barthlott, C., Adler, B., Kalthoff, N., Handwerker, J., Kohler, M., & Wieser, A. (2016). The role of Corsica in initiating nocturnal offshore convection. *Quarterly Journal of the Royal Meteorological Society*, *142*(S1), 222–237. https://doi.org/10.1002/qj.2415

Barthlott, C., & Kirshbaum, D. J. (2013). Sensitivity of deep convection to terrain forcing over Mediterranean Islands. *Quarterly Journal of the Royal Meteorological Society*, *139*(676), 1762–1779. https://doi.org/10.1002/qj.2089

Bennett, L. J., Browning, K. A., Blyth, A. M., Parker, D. J., & Clark, P. A. (2006). A review of the initiation of precipitating convection in the United Kingdom. *Quarterly Journal of the Royal Meteorological Society*, *132*(617), 1001–1020. https://doi.org/10.1256/qj.05.54

Bessho, K., Date, K., Hayashi, M., Ikeda, A., Imai, T., Inoue, H., et al. (2016). An introduction to Himawari-8/9-Japan's new-generation geostationary meteorological satellites. *Journal of the Meteorological Society of Japan*, *94*(2), 151–183. https://doi.org/10.2151/jmsj.2016-009

Brunet, G., Parsons, D. B., Ivanov, D., Lee, B. R., Bauer, P., Bernier, N. B., et al. (2023). Advancing weather and climate forecasting for our changing world. *Bulletin of the American Meteorological Society*, *104*(4), E909–E927. https://doi.org/10.1175/bams-d-21-0262.1

Carbone, R. E., Wilson, J. W., Keenan, T. D., & Hacker, J. M. (2000). Tropical island convection in the absence of significant topography. Part I: Life cycle of diurnally forced convection. *Monthly Weather Review*, *128*(10), 3459–3480. https://doi.org/10.1175/1520-0493(2000)128<3459:ticita>2.0.co;2

Chatterjee, S., & Hadi, A. S. (2006). *Regression analysis by example* (4th ed.). John Wiley & Sons.

Chen, X., Zhang, F., & Zhao, K. (2016). Diurnal variations of the land–sea breeze and its related precipitation over South China. *Journal of the Atmospheric Sciences*, *73*(12), 4793–4815. https://doi.org/10.1175/jas-d-16-0106.1

Chen, X. C., Zhang, F. Q., & Zhao, K. (2017). Influence of monsoonal wind speed and moisture content on intensity and diurnal variations of the Mei-Yu season coastal rainfall over South China. *Journal of the Atmospheric Sciences*, *74*(9), 2835–2856. https://doi.org/10.1175/jas-d-17-0081.1

Duan, Z., Zhao, B., Fu, S., Zhang, S., Lin, L., & Tang, J. (2023). Investigating the diurnal variation in coastal boundary layer winds on Hainan Island using three tower observations. *Atmosphere*, *14*(4), 751. https://doi.org/10.3390/atmos14040751

Dudhia, J. (1989). Numerical study of convection observed during the winter monsoon experiment using a mesoscale two-dimensional model. *Journal of the Atmospheric Sciences*, *46*(20), 3077–3107. https://doi.org/10.1175/1520-0469(1989)046<3077:nsocod>2.0.co;2

Esteban, M. A., & Chen, Y. L. (2008). The impact of trade wind strength on precipitation over the windward side of the Island of Hawaii. *Monthly Weather Review*, *136*(3), 913–928. https://doi.org/10.1175/2007mwr2059.1

Fovell, R. G. (2005). Convective initiation ahead of the sea-breeze front. *Monthly Weather Review*, *133*(1), 264–278. https://doi.org/10.1175/mwr-2852.1

Fu, S. Z., Rotunno, R., Chen, J. H., Deng, X., & Xue, H. W. (2021). A large-eddy simulation study of deep-convection initiation through the collision of two sea-breeze fronts. *Atmospheric Chemistry and Physics*, *21*(12), 9289–9308. https://doi.org/10.5194/acp-21-9289-2021

Gong, M., Fu, S., Liu, J., & Deng, X. (2025). A modeling study of the topographic effects on shallow convective clouds. *Earth and Space Science*, *12*(2), e2024EA003867. https://doi.org/10.1029/2024ea003867

Guillod, B. P., Orlowsky, B., Miralles, D. G., Teuling, A. J., & Seneviratne, S. I. (2015). Reconciling spatial and temporal soil moisture effects on afternoon rainfall. *Nature Communications*, *6*(1), 6443. https://doi.org/10.1038/ncomms7443

Gupta, S., Wang, D., Giangrande, S. E., Biscaro, T. S., & Jensen, M. P. (2024). Lifecycle of updrafts and mass flux in isolated deep convection over the Amazon rainforest: Insights from cell tracking. *Atmospheric Chemistry and Physics*, *24*(7), 4487–4510. https://doi.org/10.5194/acp-24-4487-2024

Hong, S. Y., & Lim, J.-O. J. (2006). The WRF single-moment 6-class microphysics scheme (WSM6). *Asia-pacific Journal of Atmospheric Sciences*, *42*, 129–151.

Hong, S. Y., Noh, Y., & Dudhia, J. (2006). A new vertical diffusion package with an explicit treatment of entrainment processes. *Monthly Weather Review*, *134*(9), 2318–2341. https://doi.org/10.1175/mwr3199.1

Huang, Q., Cai, X.-H., Song, Y., & Kang, L. (2016). A numerical study of sea breeze and spatiotemporal variation in the coastal atmospheric boundary layer at Hainan Island, China. *Boundary-Layer Meteorology*, *161*(3), 543–560. https://doi.org/10.1007/s10546-016-0177-2

Huang, Y., Meng, Z., Li, J., Li, W., Bai, L., Zhang, M., & Wang, X. (2017). Distribution and variability of satellite-derived signals of isolated convection initiation events over central Eastern China. *Journal of Geophysical Research-Atmospheres*, *122*(21), 11357–11373. https://doi.org/10.1002/2017jd026946

Iacono, M. J., Delamere, J. S., Mlawer, E. J., Shephard, M. W., Clough, S. A., & Collins, W. D. (2008). Radiative forcing by long-lived greenhouse gases: Calculations with the AER radiative transfer models. *Journal of Geophysical Research*, *113*(D13). https://doi.org/10.1029/2008jd009944

Kirshbaum, D. J., & Smith, R. B. (2009). Orographic precipitation in the tropics: Large-eddy simulations and theory. *Journal of the Atmospheric Sciences*, *66*(9), 2559–2578. https://doi.org/10.1175/2009jas2990.1

Kuo, Y. H., & Chen, G. T. J. (1990). The Taiwan area mesoscale experiment (TAMEX)—An overview. *Bulletin of the American Meteorological Society*, *71*(4), 488–503. https://doi.org/10.1175/1520-0477(1990)071<0488:ttamea>2.0.co;2

Li, Y., Liu, Y., Chen, Y., Chen, B., Zhang, X., Wang, W., et al. (2021). Characteristics of deep convective systems and initiation during warm seasons over China and its vicinity. *Remote Sensing*, *13*(21), 4289. https://doi.org/10.3390/rs13214289

Liang, Z., & Li, L.-j. (2024). What primarily regulates the evolution of convection in Hainan Island? *Atmospheric Research*, *303*, 107317. https://doi.org/10.1016/j.atmosres.2024.107319

Liang, Z., & Wang, D. (2017). Sea breeze and precipitation over Hainan Island. *Quarterly Journal of the Royal Meteorological Society*, *143*(702), 137–151. https://doi.org/10.1002/qj.2952

Liang, Z., Wang, D., Liu, Y., & Cai, Q. (2017). A numerical study of the convection triggering and propagation associated with sea breeze circulation over Hainan Island. *Journal of Geophysical Research-Atmospheres*, *122*(16), 8567–8592. https://doi.org/10.1002/2016jd025915

Lu, G. (2026). Location and time of DCI events identified on Hainan Island and Leizhou Peninsula during MJJAS of 2016–2022 [Dataset]. *Zenodo*. https://zenodo.org/records/18368323

Lu, G., Kirshbaum, D. J., & Xue, H. (2025). The role of orography on convection initiation over Hainan Island. *Quarterly Journal of the Royal Meteorological Society*, *151*(773), e5068. https://doi.org/10.1002/qj.5068

Lu, G., Ren, Y., Fu, S., & Xue, H. (2023). Statistics of isolated deep convection initiation and its relation to topography in the North China Area. *Journal of Geophysical Research-Atmospheres*, *128*(15), e2022JD037949. https://doi.org/10.1029/2022jd037949

Markowski, P., & Richardson, Y. (2010). *Mesoscale meteorology in midlatitudes*. Wiley.

NCEI. (2022). National centers for environmental information, N. W. S., NOAA, U.S. Department of commerce. ETOPO 2022 15 arc-second global relief model. Retrieved from https://www.ncei.noaa.gov/products/etopo-global-relief-model

NCEP. (2000). National centers for environmental prediction, N. W. S., NOAA, U.S. Department of commerce. FNL operational model global tropospheric analyses, continuing from July 1999. Retrieved from https://rda.ucar.edu/datasets/dsd083002/

Nugent, A. D., Smith, R. B., & Minder, J. R. (2014). Wind speed control of tropical orographic convection. *Journal of the Atmospheric Sciences*, *71*(7), 2695–2712. https://doi.org/10.1175/jas-d-13-0399.1

O'Mahony, M. (1986). *Sensory evaluation of food: Statistical methods and procedures* (1 Ed.). Routledge. CRC Press.

Perlin, N., & Alpert, P. (2001). Effects of land-use modification on potential increase of convection: A numerical mesoscale study over South Israel. *Journal of Geophysical Research*, *106*(D19), 22621–22634. https://doi.org/10.1029/2000jd900804

Qian, J. H. (2008). Why precipitation is mostly concentrated over islands in the Maritime continent. *Journal of the Atmospheric Sciences*, *65*(4), 1428–1441. https://doi.org/10.1175/2007jas2422.1

Qian, T. T., Epifanio, C. C., & Zhang, F. Q. (2012). Topographic effects on the tropical land and sea breeze. *Journal of the Atmospheric Sciences*, *69*(1), 130–149. https://doi.org/10.1175/jas-d-11-011.1

Schneider, L., Barthlott, C., Barrett, A. I., & Hoose, C. (2018). The precipitation response to variable terrain forcing over low Mountain ranges in different weather regimes. *Quarterly Journal of the Royal Meteorological Society*, *144*(713), 970–989. https://doi.org/10.1002/qj.3250

Skamarock, W., Klemp, J. B., Dudhia, J., Gill, D. O., Barker, D. M., Wang, W., & Powers, G. J. (2008). *A description of the advanced research WRF version 2*. TN-468. NCAR: Boulder. Technical Report.

Smith, R. B., Minder, J. R., Nugent, A. D., Storelvmo, T., Kirshbaum, D. J., Warren, R., et al. (2012). Orographic precipitation in the tropics the Dominica experiment. *Bulletin of the American Meteorological Society*, *93*(10), 1567–1579. https://doi.org/10.1175/bams-d-11-00194.1

Smith, R. B., Schafer, P., Kirshbaum, D. J., & Regina, E. (2009). Orographic precipitation in the tropics: Experiments in Dominica. *Journal of the Atmospheric Sciences*, *66*(6), 1698–1716. https://doi.org/10.1175/2008jas2920.1

Student. (1908). The probable error of a mean. *Biometrika*, *6*, 1–25. https://doi.org/10.2307/2331554

Trier, S. B., Davis, C. A., & Ahijevych, D. A. (2010). Environmental controls on the simulated diurnal cycle of warm-season precipitation in the continental United States. *Journal of the Atmospheric Sciences*, *67*(4), 1066–1090. https://doi.org/10.1175/2009jas3247.1

Tu, X. L., Zhou, M. Y., & Sheng, S. H. (1993). The mesoscale numerical simulation of the flow field of the Hainan Island and the Leizhou Peninsula. *Acta Oceanologica Sinica*, *12*(2), 219–235.

Walker, J. R., MacKenzie, W. M., Jr., Mecikalski, J. R., & Jewett, C. P. (2012). An enhanced geostationary satellite-based convective initiation algorithm for 0-2-h nowcasting with object tracking. *Journal of Applied Meteorology and Climatology*, *51*(11), 1931–1949. https://doi.org/10.1175/jamc-d-11-0246.1

Wang, C. C., & Kirshbaum, D. J. (2015). Thermally forced convection over a mountainous tropical Island. *Journal of the Atmospheric Sciences*, *72*(6), 2484–2506. https://doi.org/10.1175/jas-d-14-0325.1

Wang, Y., Miao, J., & Su, T. (2018). A numerical study of impact of topography on intensity and pattern of sea breeze precipitation over the Hainan Island. *Plateau Meteorology*, *37*(1), 207–222.

Yang, Y., & Chen, Y. L. (2008). Effects of terrain heights and sizes on island-scale circulations and rainfall for the island of Hawaii during HaRP. *Monthly Weather Review*, *136*(1), 120–146. https://doi.org/10.1175/2007mwr1984.1

Yeh, H. C., & Chen, Y. L. (1998). Characteristics of rainfall distributions over Taiwan during the Taiwan area Mesoscale experiment (TAMEX). *Journal of Applied Meteorology*, *37*(11), 1457–1469. https://doi.org/10.1175/1520-0450(1998)037<1457:cordot>2.0.co;2

Zadra, A., Williams, K., Frassoni, A., Rixen, M., Adames, A. F., Berner, J., et al. (2018). Systematic errors in weather and climate models: Nature, origins, and ways forward. *Bulletin of the American Meteorological Society*, *99*(4), ES67–ES70. https://doi.org/10.1175/bams-d-17-0287.1

Zhang, J., Zhu, W. B., Zhao, F., Zhu, L. Q., Li, M. J., Zhu, M., & Zhang, X. D. (2018). Spatial variations of terrain and their impacts on landscape patterns in the transition zone from mountains to plains: A case study of Qihe River basin in the Taihang Mountains. *Science China Earth Sciences*, *61*(4), 450–461. https://doi.org/10.1007/s11430-016-9158-2

Zhang, J., Zhu, W. B., Zhu, L. Q., Cui, Y. P., He, S. S., & Ren, H. (2019). Topographical relief characteristics and its impact on population and economy: A case study of the mountainous area in western Henan, China. *Journal of Geographical Sciences*, *29*(4), 598–612. https://doi.org/10.1007/s11442-019-1617-y

Zhang, Y., Sun, J., & Fu, S. (2013). Impacts of diurnal variation of mountain-plain solenoid circulations on precipitation and vortices east of the Tibetan Plateau during the mei-yu season. *Advances in Atmospheric Sciences*, *31*(1), 139–153. https://doi.org/10.1007/s00376-013-2052-0

Zhang, Z. Z., Cao, C. X., Song, Y., Kang, L., & Cai, X. H. (2014). Statistical characteristics and numerical simulation of sea-land breezes in Hainan Island. *Journal of Tropical Meteorology*, *20*(3), 267–278.

Zhu, L., Bai, L. Q., Chen, G. X., Sun, Y. Q., & Meng, Z. Y. (2021). Convection initiation associated with ambient winds and local circulations over a tropical Island in South China. *Geophysical Research Letters*, *48*(16), e2021GL094382. https://doi.org/10.1029/2021gl094382

Zhu, L., Chen, X. C., & Bai, L. Q. (2020). Relative roles of low-level wind speed and moisture in the diurnal cycle of rainfall over a tropical island under monsoonal flows. *Geophysical Research Letters*, *47*(8), e2020GL087467. https://doi.org/10.1029/2020gl087467

Zhu, L., Meng, Z. Y., Zhang, F. Q., & Markowski, P. M. (2017). The influence of sea- and land-breeze circulations on the diurnal variability in precipitation over a tropical island. *Atmospheric Chemistry and Physics*, *17*(21), 13213–13232. https://doi.org/10.5194/acp-17-13213-2017

Zhuge, X. Y., & Zou, X. L. (2018). Summertime convective initiation nowcasting over southeastern China based on advanced Himawari imager observations. *Journal of the Meteorological Society of Japan*, *96*(4), 337–353. https://doi.org/10.2151/jmsj.2018-041

Ziegler, C. L. (2014). Deep convection initiation: State of the science, limits of understanding, and future directions. In *Paper presented at the paper presented at the 94th American meteorological society annual meeting*. Retrieved from https://ams.confex.com/ams/94Annual/webprogram/Paper236651.html

Zinner, T., Mannstein, H., & Tafferner, A. (2008). Cb-TRAM: Tracking and monitoring severe convection from onset over rapid development to mature phase using multi-channel Meteosat-8 SEVIRI data. *Meteorology and Atmospheric Physics*, *101*(3–4), 191–210. https://doi.org/10.1007/s00703-008-0290-y